Computation of Effective Permeability for Porous Carbon Composites

Savio J. Poovathingal*, Brendan M. Soto, Cameron Brewer

Department of Mechanical Engineering, University of Kentucky, Lexington, KY, USA 40506.

Abstract

Effective permeability of a porous carbon composite is computed using the direct simulation Monte Carlo technique. The microstructure of the carbon composite is synthetically generated using an in-house solver. Permeabilities obtained using synthetic microstructures of the precursor (carbon fibers) is compared to two independent experimental dataset and good agreement is observed. An approach to digitally infuse matrix into the precursor is proposed. Comparison of the permeability for the full composite (carbon fibers with matrix) with experimental data demonstrates good agreement indicating that representative microstructures generated digitally can be used to compute and predict effective permeability of porous carbon composites. Simulations of gases penetrating the full composite are performed, and an intrinsic material permeability (K_o) of 11.866×10^{-11} m^2, and a Klinkenberg constant (b^*) of 5.655×10^{-8} that is only dependent on the temperature and the molecular weight of the gaseous species is obtained.

1. Introduction

Porous materials have many present and potential future applications for catalysis, adsorption and separation, life science, energy, environmental and high-end technologies [1]. Effective permeability is an important property of a

*Corresponding author
Email address: saviopoovathingal@uky.edu (Savio J. Poovathingal)

porous material as it dictates the flow of gases and liquids through the pores of the material. Effective permeability is used as a design property for extracting shale gas in the energy sector [2] and for molecular sieves for filtration [3]. Effective permeability is also an important property for carbon composites that are used as thermal protection systems (TPS) to mitigate the heat load during the entry process of a space capsule.

Carbon composites used as TPS materials are low-density materials that consist of a network of carbon fibers infused with a resin (also referred to as the matrix). These materials relieve heat load through a number of processes, including absorption processes such as thermochemical decomposition of the filler resin and sublimation, and heat rejection processes through modification of the high-temperature boundary layer through transpiration of ablation products, and systematic sacrificial removal of hot material through ablation [4]. The composites used on space capsules are highly porous with the fiber and resin occupying not more than 20% of the total volume. The high porosity allows gases to flow through the material. For example, the resin decomposes (process called pyrolysis) and travels through the charred (completely pyrolyzed) network of fibers. Similarly, boundary layer gases can penetrate the material causing in-depth gas-phase and gas-surface reactions [5]. Flow through TPS materials are computed by solving the combined solid-gas momentum transport equations. Historically, the momentum transport equations have been formulated as either surface models, one-dimensional volume averaged models [6, 7], and more recently have been formulated as two/three-dimensional volume averaged models [8–16]. Such volume-averaged approaches [17] for momentum transport require model closure, in this case, the effective permeability of the material. Since the entry process occur at high altitudes, the flow inside these carbon composites occur in the non-continuum regime. The analysis of Stardust trajectory indicates that the flow is either in the transition or slip regime while it flows through the pores of the carbon composite [18]. Therefore, analytical relations that are derived either in the continuum or the free-molecular limit cannot be used as the effective permeability for flight relevant conditions.

A widely used carbon composite on various space missions consists of a carbon fiber network called FiberForm (manufactured by FiberMaterials Inc.) into which a phenolic resin is infused. FiberForm is manufactured by chopping fibers and pressing them into billets which creates a random network of fibers with a preferential direction normal to the pressing plane creating an orthotropic material. The resin is infused into this network which attaches to the fibers. Effective permeability for FiberForm and the full composite has been obtained empirically by Marschall and Milos [19, 20]. Marschall and Milos performed the experiments using a flow tube apparatus with air as the test gas and all experiments were performed at room temperature. Recently, Panerai et al. [5] performed flow tube experiments to obtain effective permeability of FiberForm over nine different samples with different densities at different temperatures using Ar as the test gas. They found significant variability in the permeability values for different samples.

Effective permeability of FiberForm has been computationally obtained by various groups [21–26]. Borner et al. [21], White et al. [22], and Jambunathan et al. [23] used direct simulation Monte Carlo (DSMC) as the flow solver while Ho et al. [26, 27] used Lattice Boltzmann as the flow solver. In most of these cases, the microstructure of FiberForm was imported from x-ray computed tomography (XRCT) images of the FiberForm sample. Since XRCT images were obtained only for a few samples, it limits the validation efforts with experiments and the ability to explore the material parameter space that influences effective permeability. Stern et al. [25] developed a synthetic microstructure generating code called Fibergen to reproduce the microstructure of FiberForm. Effective permeability of the synthetically generated microstructure was computed through DSMC simulations using the molecular gas dynamics solver [24]. It was shown that the microstructures of FiberForm generated using Fibergen reproduced the experimental results of Marschall and Milos [19]. Since Fibergen is a computational code, several parameters of the code can be controlled, allowing a systematic study of the parameters that influence effective material properties. A systematic study was performed by the authors by varying the

fiber radius and elevation angles. It was found that a fiber radius of 5 μm and an elevation angle of 25° resulted in the best agreement between the experiments and simulations. However, it was also observed that moderate variations in fiber radius, angle, and the inherent randomness in fiber arrangement combine to give approximately ±30% variation in the computed effective permeability value for a given pressure condition. The comparisons of permeability for microstructures generated using Fibergen in the previous study was limited to the data of Marschall and Milos [19].

The objective of this article is twofold. New DSMC simulations are performed to compute effective permeability using synthetic microstructures generated from Fibergen to demonstrate the wider applicability of using synthetic microstructures. The effective permeability computed from the DSMC simulations are compared against the experimental dataset of Panerai et al. [5]. Second, a method to synthetically infuse resin is proposed and this approach is validated against experimental data that is available for the full composite (FiberForm infused with resin) [20]. All previous computational work have been limited to computing the permeability of FiberForm. It is also shown that an expression developed for FiberForm [5] can be extended to the full composite and effective permeability values are derived that can be used in computational fluid dynamics (CFD) or material response solvers.

2. Methods

Synthetic microstructures are generated using the Fibergen code and the permeability calculations are performed using the DSMC technique. Both approaches are briefly discussed in this section. A more detailed description of the code layouts, efficiency considerations, and coupling strategies can be found in previous publications [24, 25].

2.1. Fibergen: A Synthetic Microstructure Generating Code

Fibergen uses dimensions of the domain to be simulated (also referred to as box in this article), target bulk porosity, nominal fiber orientation, nominal

fiber radius, and specified variances to generate cylindrical fibers. To replicate the FiberForm microstructure, the radius of a cylindrical fiber is sampled from a Gaussian distribution with a mean of 5 μm and standard deviation of 0.1 μm [28]. FiberForm is orthotropic because of the manufacturing process wherein fibers are pressed into billets. This pressing affects the fiber angles because they have a bias toward being oriented parallel to the pressing plane (also referred to as the through the thickness plane) [24]. Therefore, elevation angle of the fiber is sampled from a uniform distribution of $\pm 25^{\circ}$. The nominal fiber radius, elevation angle, and the standard deviations are chosen based on the conclusions of the parametric study performed previously [24]. After the first cylindrical fiber is generated, successive fibers are added only if the new fiber does not intersect or overlap with other fibers in the domain. Previously, fibers were generated until a target porosity was attained. Several details of the Fibergen code along with the algorithm, code layout and architecture have been described before and is available in Ref. 25. Two new features have been added to Fibergen which are described below.

First, fibers can now be generated until a target sample density is attained. In this mode, Fibergen uses the density of a single carbon fiber as an input and fibers are generated in the same manner as described above until the density of the simulated box reaches a target value. Data from Panerai et al. [5] is available for eight samples with different densities. Therefore, modifying the convergent criteria of Fibergen allows a direct comparison with experimental data of Panerai et al. [5]. A sample microstructure generated using Fibergen is shown in Fig. 1a. The choice of density for an individual fiber is discussed in Sec. 3. Previously, Fibergen created surface triangles on the fibers that can be used as the surface mesh in the DSMC solver. The second new feature that is added is to allow the output of the microstructure in three-dimensional voxel format. In the voxel format, a three-dimensional box containing the fibers are discretized to a desired resolution. Nodal points inside and outside the fibers are marked as 1 and 0, respectively. This voxelized feature is leveraged to incorporate resin into the microstructure. A sample microstructure generated

at a voxel resolution of 2.5 μm without the resin is shown in Fig. 1b.

To incorporate the resin, the fibers are initially generated as described above. The box containing the fibers is discretized to a desired resolution and the volume occupied by the fibers in each cell is computed using the cut-cell technique [29]. In the manufacturing of the composite, the resin is infused into the microstructure of FiberForm which bonds to the carbon fibers in a random manner. Since the resin randomly infuses into the composite, a similar approach is taken here. A discretized cell within the three-dimensional box is chosen randomly. Cells that are completely inside the fiber or that do not contain any fiber (no cut-volume) are ignored and a new cell is chosen until a cell with partially occupied fiber is selected. The volume occupied by the fiber inside the cell is known through the cut-cell technique [29] and the resin is added to the remaining volume. All corners of the chosen cell are marked as 1 which assumes that the entire remaining volume is occupied by the resin. Resin is added until the density of the composite reaches the target value. The final voxelized mesh is used as the input into the DSMC solver. A sample microstructure generated at a voxel resolution of 2.5 μm with the resin is shown in Fig. 1c.

2.2. Sparta: DSMC Solver

The numerical investigation is performed using the DSMC technique. The DSMC technique is a stochastic approach that simulates the Boltzmann equation. A detailed description of the DSMC technique and models can be found in Refs. 30, 31. The relevance and advantage of using the DSMC technique to compute effective properties for porous TPS materials can be found in Refs. 24, 25. The DSMC simulations are performed using the open-source DSMC solver Stochastic Parallel Rarefied-gas Time-accurate Analyzer (SPARTA) [32–34], which uses a multi-level Cartesian mesh to track and collide particles. Surfaces can be identified in two ways. A set of triangles representing the surfaces is directly read into Sparta or a set of voxels are converted to a closed surface with triangles using the marching cube algorithm [32, 35]. The triangles are sorted (for marching cube, sorting is not required) and the flow volume in

each cell is computed using the cut-cell technique. Both approaches are used to import microstructures of FiberForm (see Sec. 3 for related discussion). The standard ray-tracing approach is used to move the simulation particles.

The flow setup for the permeability simulations is shown in Fig. 1d. As seen from Fig. 1d, the microstructure is incorporated into the center of the simulated domain. Symmetric boundary conditions are applied in the two span-wise directions (y and z). In the upstream boundary, pressure (P_{in}) and temperature (T) are specified. The inflow velocity (u) is obtained using a simple zeroth order extrapolation, i.e. u =u_j, where j refers to the value at the first interior cell. In the downstream boundary, the method of characteristics of Nance et al. [36] and Fang and Liou [37] is used. Specifically, the outflow pressure (P_{out}) is specified and the remaining macroscopic properties are computed using information from the interior solution. The relevant equations to obtain the boundary information are available in Refs. [25, 36, 37]. These boundary conditions have been validated in the previous study [24]. For the mean flow quantities from the interior cell, instantaneous mean flow quantities can be used or a sub-relaxation averaging can be applied [25]. We found that both approaches provide the same accuracy but the sub-relaxation technique is more stable and robust.

The simulations are run until steady state and a permeability force F is computed as described in Marschall and Milos [19] (Eqn. 1).

$$F \equiv \frac{\mu \dot{m} T R L}{A M \Delta P} = K_0 (P_{av} + b) \ , \tag{1}$$

In Eqn. 1, F is the permeability force, μ is the viscosity, $\dot{m}$ is the mass flow rate, T is the temperature, R is the universal gas constant, L is the length of the sample, A is the area, M is the molecular mass, ΔP is the pressure difference across the sample, K_0 is the permeability in the continuum limit, and b is the Klinkenberg constant. A power-law viscosity model is used to compute F, which is shown in Eqn. 2.

$$\mu = \frac{15\sqrt{\pi m k T_{ref}}}{2(5-2\omega)(7-2\omega)\pi d_{ref}^2} \left(\frac{T}{T_{ref}} \right)^{\omega} \tag{2}$$

In Eqn. 2, k is the Boltzmann constant, T_{ref} is a reference temperature of 273 K, d_{ref} is the reference diameter, and ω is the variable hard sphere (VHS) exponent. The reference diameter (d_{ref}) of Ar, N_2, and O_2 are 4.17×10^{-10}, 4.17×10^{-10}, and 3.96×10^{-10} m, respectively. The VHS exponent of Ar, N_2, and O_2 are 0.81, 0.77, and 0.74 respectively. We note here that viscosity is not directly used in DSMC simulations but rather through the specification of d_{ref} and the VHS exponent.

The physical meaning and derivation of Eqn. 1 can be found in Refs. [5, 24]. In the experiments [5, 19, 20], F is plotted as a function of P_{avg} and a curve fit is performed to obtain K_o and b. K_o depends on the geometric property of the material (arrangement of fibers and resin) and b depends on the type of gas and flow temperature. As discussed in Sec. 3, in the validation step, we compare the value of F directly with experimental data. When new data is generated for the full composite, a linear least square fit is performed to obtain K_o and b. This formulation for the effective permeability follows the Klinkenberg formulation, which is given in Eqn. 3.

$$K = K_o \left(1 + \frac{8c}{d_p}\lambda\right) \tag{3}$$

In Eqn. 3, K_o is the permeability constant, d_p is the pore diameter, λ is the mean free path, and c is a proportionality constant.

3. Results

3.1. Permeability computations of FiberForm

In all simulations discussed in this article, a nominal pressure difference of 100 Pa is prescribed for the boundary conditions. For example, for an average pressure (P_{avg}) of 500 Pa, P_{in} and P_{out} is set to 550 and 450 Pa, respectively. The flow is allowed to evolve based on the boundary conditions. The final P_{avg} and ΔP are then computed by extracting the pressure before and after the sample. Therefore, the final P_{avg} and ΔP will not be exactly equal to the specified values, although it will be close to the specified values. A convergence

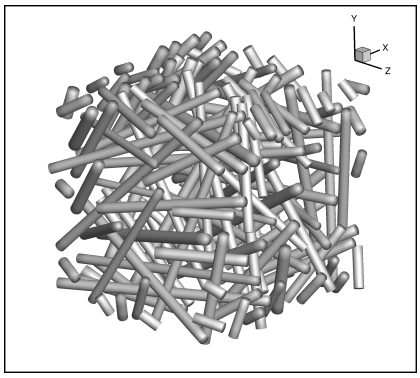

(a) Surface mesh for a microstructure generated as a set of triangles.

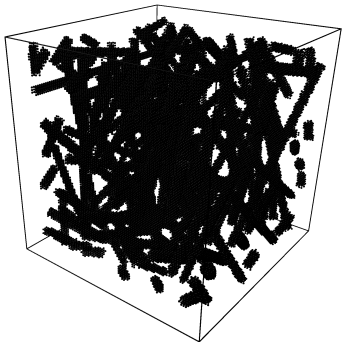

(b) Voxel representation of a microstructure without resin at a resolution of $2.5\mu m$.

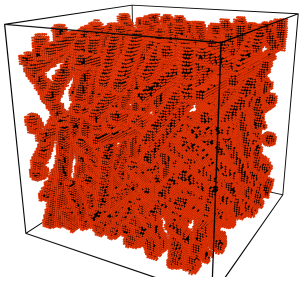

(c) Voxel representation of a microstructure with resin at a resolution of $2.5\mu m$.

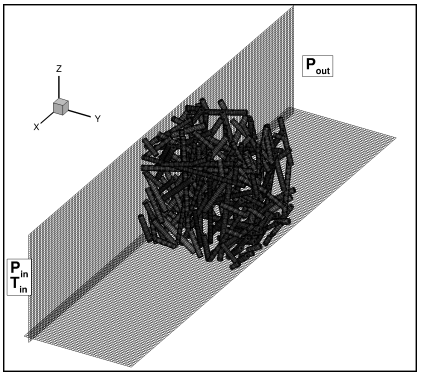

(d) Flow setup for all simulations.

Figure 1: Surface meshes and flow setup schematic for all simulations. In Figs. 1b and 1c, black voxels represent carbon fibers, while the red voxels in Fig. 1c represents the resin.

test is initially performed on the size of the microstructure that needs to be simulated. This is referred to as the representative elementary volume (REV). Microstructures are generated with a fixed target porosity of 0.9. Box size in the span-wise direction is varied between $125 - 300\ \mu m$ and between $200 - 500\ \mu m$ in the flow direction (the through thickness direction). P_{avg}, ΔP, and F for all cases are shown in Table 1 along with the error which is computed in comparison with a microstructure with a domain size of $500 \times 300 \times 300\ \mu m$. For the simulations described in Table 1, Ar is used as the test gas. It is observed that the error is low once the REV is at least $200 \times 200 \times 200\ \mu m$. It would

appear that the error is higher with a box size of $500 \times 250 \times 250\ \mu m$ compared to a box size of $500 \times 200 \times 200\ \mu m$ (entries 2 and 3 in Table 1) but it is merely an artifact of the variability of FiberForm. A dominant feature of FiberForm microstructure is the variability in the material properties [5] as seen in experiments and our previous computations [24]. Fibergen attempts to capture this effect by sampling over distributions in a stochastic manner. Changes in the overall domain size will result in small changes in how the fibers are arranged, which in turn influences the effective permeability. It was previously observed that moderate changes in the fiber radii and elevation angles result in variations up to $\pm 30\%$ [24]. Therefore, all simulations with low error are equally valid solutions with sufficient accuracy. To balance REV size with computational load, an REV of $200 \times 200 \times 200\ \mu m$ is used for all the simulations in this article. The REV is used to perform a convergence test on the DSMC simulations for the number of simulated particles (N_p) , cell resolution (Δx), and timestep (Δt). Based on the convergence test, $N_p = 50$, $\Delta x = \frac{\lambda}{2}$, $\Delta t = \frac{\tau}{20}$ is used where λ is the mean free path and τ is the mean collision time. A convergence test is also performed on the number of time steps simulated until steady state and the number of timesteps over which mean flow mean quantities are averaged. Convergence is obtained by running simulations for 100,000 timesteps until steady state and averaged for an additional 100,000 timesteps. The simulated domain in the x-direction is $600\ \mu m$ with $200\ \mu m$ on either side (equal to the REV length) and a convergence test is also performed on the required domain length in the x-direction.

Next, the effect of sample density on the permeability force (F) is examined. As discussed in Sec. 2.1, Fibergen uses individual fiber density as an input to generate a microstructure with a target sample density. FiberForm is manufactured from rayon-based fibers for which the individual fiber density varies from $1400 - 1700$ kg m^{-3} [38]. For a given sample density, a higher individual fiber density results in lower number of fibers inserted into the REV resulting in higher porosity, thereby making the microstructure more permeable. The permeability force F obtained for a sample density of 181 and 157 kg m^{-3}, and

Table 1: Permeability force (F) obtained with various REV sizes. All error is computed with reference to an REV size of 500 $\times$ 300 $\times$ 300 μm for which the force, F = 1.378e-7 N.

Microstructure size (in μm) X x Y x Z	P_{avg} (Pa)	ΔP (Pa)	F (N)	Absolute Error (%)
500 x 125 x 125	533.5	77.06	1.69e-07	22.74
500 x 200 x 200	514.6	90.19	1.417e-07	2.4
500 x 250 x 250	509.74	93.41	1.343e-07	2.68
200 x 125 x 125	535.0	74.67	1.734e-07	25.64
200 x 200 x 200	515	89.6	1.45e-07	5.3
200 x 250 x 250	521.96	86.86	1.45e-07	5.3
200 x 300 x 300	507.14	95.18	1.404e-07	1.673

fiber densities varying from $1400 - 1700$ kg m^{-3} is shown in Table 2. The corresponding porosity is also shown in Table 2 for reference. For all simulations in Table 2, P_{in} and P_{out} is set to 550 and 450 Pa, respectively and flow temperature is set to 297 K. Ar is used as the test gas for the simulations with a sample density of 181 kg m^{-3} while air is used for computing the permeability for the sample density of 157 kg m^{-3}. These test gases correspond to the appropriate gases used in the experimental study. As expected, it is seen that for a given sample density, lower values of F are obtained when the fiber density is lower (material is less permeable). The sample density of 157 kg m^{-3} corresponds to one of the experimental data of Marschall and Milos [19], while the sample density of 181 kg m^{-3} corresponds to the dataset of Panerai et al. [5]. First, we observe that small changes in porosity result in huge variations in the permeability values, which reinforces the conclusion that effective properties of FiberForm exhibit high variability. Panerai et al. used the average density of all the experimental samples and the reported open porosity of FiberForm to estimate the fiber density as 1400 kg m^{-3}. We also see excellent agreement between the experimental data and the simulation results with an individual fiber

density of 1400 kg m^{-3}. Specifically, we are able to capture the permeability force for independent datasets of Marschall and Milos [19] and Panerai et al. [5] merely by specifying the sample density. In the dataset of Panerai et al., two samples (TT04 and TT09) with the same sample density of 181 kg m^{-3} result in drastically different permeability values [5] (see Table 1 of Ref. [5]). The permeability force (F) of sample TT09 is very high and can be reproduced only with a porosity of 0.91. Such variability is expected in FiberForm and could also arise from defects and impurities [28]. To assess the robustness of Fibergen and the DSMC simulations, the comparison of the DSMC simulations with all of the experimental data of Panerai et al. is shown in Table A.3 in the appendix. While the average pressure for most simulations correspond to 500 Pa, some cases are also simulated at 250 Pa to assess if the DSMC simulations capture the effective permeability values at different pressures. The flow temperature corresponds to the appropriate experimental value (Table 1 of Ref. [5]). It is observed that the experimental values are being reproduced over a wide range of sample densities and temperatures. There is a systematic trend in some samples where the error is higher at lower pressures and higher temperatures. Consider the sample at a density of 181 kg m^{-3} (entry 4 in Table A.3) where the error is 0.8% at 297 K, but at 723 K, it is 29% and 37% for an average pressure of 500 and 250 Pa, respectively. There are two possible reasons for this discrepancy. The experiments were performed at higher pressures (all greater than 1000 Pa) and the experimental fit used to obtain F could lose accuracy at values outside this range. However, one would expect this error to be random and not exhibit a systematic trend based on pressure or temperature. A plausible reason is the limitation of Klinkenberg relations in the rarefied regime. The Klinkenberg formulation to which the experimental data is fit (Eqn. 3) accounts for correction related to first-order rarefaction effects. Beskok et al. [39] have derived a second-order correction factor (f_c) for the permeability, given by Eqn. 4. In Eqn. 4, Kn is the Knudsen number, α and b are constants [40]. The Klinkenberg formulation only accounts for the $(1+\alpha Kn)$ term. All values predicted from the DSMC computations are higher than the experimental permeability force (es-

timated through Eqn. 1) when the error is high suggesting that a second-order correction term may be required for some of the simulated pressures and temperatures. New experiments are being planned and since pressures of 250 and 500 Pa are relevant for flight conditions [18], second-order rarefaction effects will be examined in the future. Despite a few cases with errors greater than 30%, it is seen that the experimental data is being reproduced with good accuracy for a wide range of FiberForm samples. It is important to emphasize here that the data is being reproduced through physical values of fiber density and sample densities into Fibergen as an input and not adjustable parameters. This result provides further evidence that representative microstructures generated using Fibergen can be used to compute and predict effective material properties of FiberForm.

$$f_c = [1 + \alpha Kn]\left[1 + \frac{4Kn}{1 - bKn}\right] \tag{4}$$

Table 2: Comparison of permeability force computed using DSMC simulations with the experimental data of Marschall and Milos (157 kg m^{-3}) [19] and Panerai et al.(181 kg m^{-3}) [5].

Sample density (kg/m^3)	Fiber density (kg/m^3)	Porosity (ϕ)	F$_{expt}$ (N)	F$_{dsmc}$ (N)
157	1600	0.902	1.33e-07	1.71e-07
	1400	0.887		1.38e-07
181		0.91[1]	1.19e-07[2] 1.96e-07[3]	2.01e-07
	1700	0.893		1.58e-07
	1600	0.887		1.45e-07
	1400	0.87		1.22e-07

[1] Microstructure generated with higher porosity to compare with experimental data of TT09 sample from Panerai et al.

[2] Sample TT04 in Ref. 5.

[3] Sample TT09 in Ref. 5

In the simulations described above, the microstructure was read into Sparta

as a set of triangles (herein referred to as the stl format). We now compute effective permeability by generating surfaces in the form of voxels. In the voxel representation, constructing a perfect cylinder would require infinite resolution because it attempts to reproduce the cylinders with a set of cubes. Therefore, a convergence test is performed to determine the resolution required to capture the effective permeability. A microstructure with an individual fiber density of 1400 kg m^{-3} and sample density of 157 kg m^{-3} is generated with an REV size of 200 $\times$ 200 $\times$ 200 μm. The surface mesh is generated at a resolution of 5, 2.5, and 1.25 μm respectively. The permeability force computed at a nominal average pressure of 500 Pa at different voxel resolution is shown in Fig. 2. The permeability force values computed by the voxel approach is lower than the stl format at all resolutions. This is expected because a voxelized cylinder diameter will always be greater than the true cylinder diameter which the stl format captures. A larger cylinder diameter implies that the pathway for the fluid is more constricted making the material less permeable (hence the lower value of F). A resolution of at least 1.25 μm is required to reduce the error to $\sim 6\%$ when voxels are used to represent the surface mesh. A similar resolution requirement was also required for lattice Boltzmann simulations [26]. A resolution of 1.25 μm results in computationally expensive calculations compared to the stl format. In DSMC simulations, the required cell size for permeability computations is $\mathcal{O}(\lambda)$. The mean free path (λ) for Ar at a pressure of 500 Pa and 300 K is 10^{-5} μm. For a total simulation domain of 600 $\times$ 200 $\times$ 200 μm, a resolution of 1.25 μm (required voxel resolution) will result in $\sim$ 12 million cells and 600 million simulation particles. While these computations are certainly feasible, the calculations consume significant compute hours. In comparison, the stl format requires only 192,000 cells (resolved to $\mathcal{O}(\lambda)$) with 10 million particles resulting in computations that are orders of magnitude faster allowing rapid computations using the stl format.

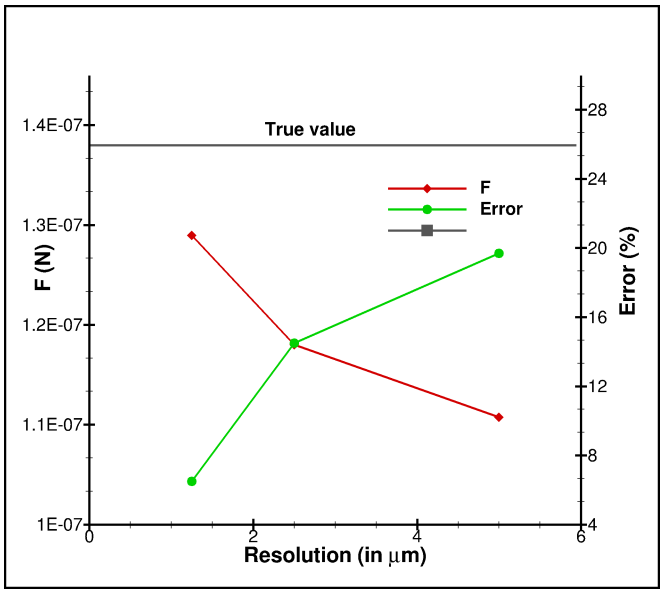

Figure 2: Permeability force computed at an average pressure of 500 Pa and 300 K with various voxel resolutions. The sample density is 157 kg m^{-3} and Ar is used as the test gas for the simulations. True value represents the force computed using the stl format.

3.2. Permeability computations of the full composite

In this section, DSMC simulations to compute effective permeability of the full composite is discussed. Although expensive, the voxel format is required for the full composite because the phenolic resin that bonds to the fibers does not form an ordered structure. The resin is infused into the FiberForm microstructure digitally through the process described in Sec. 2.1. All microstructures are generated with a resolution of 1.25 μm and the simulations are performed at 300 K with air as the test gas. The simulations of the full composite are compared to the data from Marschall and Milos [20]. The construction of the microstructure for the full composite requires the specification of the individual fiber density, FiberForm (precursor) density, phenolic resin density, and the full composite density. Marschall and Milos only provide the full composite densities [20]. For the synthetic microstructures, the individual fiber density is fixed at 1400 kg m^{-3} based on the results discussed in Sec. 3.1, and the density of phenolic resin

is set to 1200 kg m^{-3} [41].

To assess the effect of FiberForm density, microstructures are generated with FiberForm and full composite densities of 149 and 217 kg m^{-3}, respectively. It is observed that the computations over-predict the permeability force with the specified densities of 149 and 217 kg m^{-3} (red curve in Fig. 3). To assess the sensitivity, F is computed for a microstructure generated with a FiberForm density of 149 kg m^{-3} and a full composite density of 210 kg m^{-3} (pink symbol in Fig. 3). It is observed that there is no change in F when the full composite density is varied indicating that F is insensitive to small changes in the amount of resin infused into the microstructure. The volume fractions of resin added for a composite density of 210 and 217 kg m^{-3} are 0.07 and 0.09, respectively. The calculations are repeated with a sample FiberForm (precursor) density of 157 kg m^{-3}. Additionally, simulations are also performed to compute F for a microstructure generated with the density of phenolic resin set to 1400 kg m^{-3} (orange symbol in Fig. 3). A similar behavior is observed with a FiberForm density of 157 kg m^{-3}, where small changes in the amount of resin added to the microstructure does not influence the effective permeability of the composite. The FiberForm sample density for the full composite is not directly available, and it was initially estimated as 149 and 157 kg m^{-3} based on the pure FiberForm sample data (Refs. [19, 20]). The DSMC simulations indicate that small changes in the amount of resin infused does not significantly alter the effective permeability. In contrast, small changes in the FiberForm density result in significant changes in the effective permeability (see Sec. 3.1 and associated discussion). The experimental data in Fig. 3 indicates variability with minor changes in the full composite density but the trends are not consistent. The permeability force (F) of the composite with a density of 211 kg m^{-3} is lower than the composite with a density of 209 kg m^{-3} (Fig. 3). The inconsistency could arise from differences in the density of FiberForm into which the resin is infused. The permeability force F computed with a FiberForm density of 180 kg m^{-3} and a full composite density of 210 kg m^{-3} lies within 5 % of the experimental data. The FiberForm density of 180 kg m^{-3} lies within the expected range of

FiberForm densities [5, 19] suggesting that the approach of infusing resin discussed in this article does reproduce the microstructures of the full composite. However, new targeted experiments with precursor and full composite densities are required for further validation.

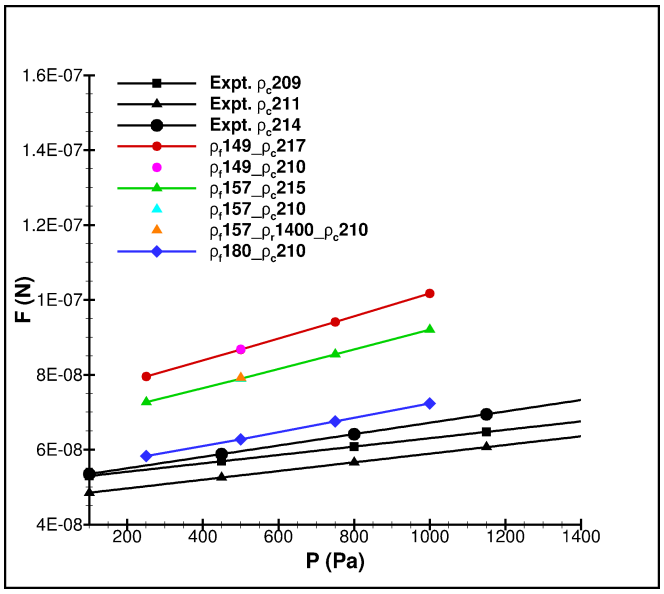

Figure 3: Comparison of DSMC simulations with experimental data of the full composite. The FiberForm, full composite, and resin density is denoted as ρ_f, ρ_c, and ρ_r, respectively.

Finally, the full composite (ρ_c = 210 kg m^{-3}) generated with a FiberForm density of 180 kg m^{-3} is used to compute the permeability force using Ar as the test gas to predict values for the Klinkenberg formulation. The approach follows the work in Ref. [5]. A constant ($\frac{b}{b^*}$) is first computed from Eqn. 5 which is used to normalize the data. In Eqns. 5, $*$ refers to a reference state, which is considered to be Ar at 300 K. The normalized force (F*) is then given by Eqn. 6. The normalized force (F*) collapses to a single curve for both Ar and air as shown in Fig. 4. A linear curve fit is performed using F* and P$_{avg}$ using data from both Ar and air to obtain new K$_o$ and b*.

$$\frac{b_i}{b^*} = \frac{\mu_i(T)}{\mu^*(T)}\sqrt{\frac{\pi}{2}\frac{RT}{M_i}}\sqrt{\frac{2}{\pi}\frac{M^*}{RT^*}} \tag{5}$$

$$F^* = K_o(P_{avg} + b^*) \tag{6}$$

The curve fit provides an effective permeability, $K_{eff} = K_o(P + b^*)$, where $K_o = 11.866 \times 10^{-11}$ m^2 and b$^* = 5.655 \times 10^{-8}$. This effective permeability is valid in the pressure range of the simulations for both Ar and air. Since the normalization is based purely on temperature, viscosity relation, and molecular weight, the derived relation could be used for other conditions. To assess the feasibility of the new relation for different conditions, the permeability for the full composite is computed with CO as the test gas at 300 K and 650 Pa resulting in $F_{dsmc} = 6.4 \times 10^{-8}$ N, while the predicted value from the new relation is 7.3×10^{-8} N (error of 11 %). The error is low in comparison to the expected variability of the material (±30%) suggesting that the new relation could be extended to other gases that have not been explicitly simulated in this article. We note here that the phenolic resin undergoes thermal decomposition ejecting a wide range of gaseous species [42]. Additional validation and refinement of this relation with different gases ejected during pyrolysis will be performed in the future.

4. Conclusion

The direct simulation Monte Carlo (DSMC) method was used to compute the effective material permeability of porous carbon composites. A synthetic microstructure generating called Fibergen was used to generate representative microstructures of the composite consisting of carbon fibers and phenolic resin. The simulations were compared against the experimental dataset of Marschall and Milos and Panerai et al. [5]. It was observed that the microstructures of FiberForm generated using Fibergen reproduced the effective permeability of both datasets with errors within 10 % at low temperatures and high pressures. A systematic increase in the error was observed at high temperatures

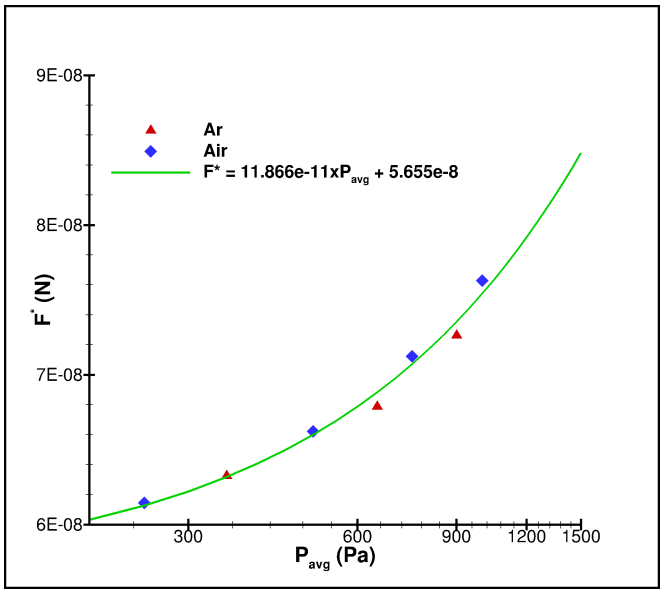

Figure 4: Normalized force (F*) and the corresponding curve fit to obtain the intrinsic permeability (K_o) and the permeability constant b*.

and low pressures for some samples, which could arise from the limitation of the Klinkenberg formulation that was used to interpret the experimental and simulation results.

The initial validation with FiberForm was extended to the full composite through a novel infusion approach for the digital microstructures. Comparison of the effective permeability with the experimental data indicated good agreement. A new relation for the effective permeability was obtained through additional DSMC simulations, and it was demonstrated that the relation could be used for gaseous species that were not explicitly simulated to derive the relation. Avenues for new targeted experiments have been identified and additional validation will be performed in the future.

5. Acknowledgements

Financial support from NASA Kentucky EPSCoR under NASA grant number 80NSSC19M0052 is acknowledged. Brendan Soto would like to acknowledge

support from NASA Kentucky Space Grant Fellowship under grant number 80NSSC20M0047. Cameron Brewer is a fellow with the Chellgren Center for Undergraduate Excellence. Insightful discussions with Dr. Alexandre Martin on the Klinkenberg formulation is deeply appreciated. We also thank the University of Kentucky Center for Computational Sciences and Information Technology Services Research Computing for their support and use of the Lipscomb Compute Cluster and associated research computing resources.

References

[1] P. Liu, G.-F. Chen, Porous materials: processing and applications, Elsevier, 2014.

[2] A. Rabbani, M. Babaei, Hybrid pore-network and lattice-boltzmann permeability modelling accelerated by machine learning, Advances in water resources 126 (2019) 116–128. doi:https://doi.org/10.1016/j.advwatres.2019.02.012.

[3] M. Carta, R. Malpass-Evans, M. Croad, Y. Rogan, J. C. Jansen, P. Bernardo, F. Bazzarelli, N. B. McKeown, An efficient polymer molecular sieve for membrane gas separations, Science 339 (6117) (2013) 303–307. doi:DOI:10.1126/science.1228032.

[4] W. H. Bowman, R. M. Lawrence, Ablative materials for high-temperature thermal protection of space vehicles, Journal of Chemical Education 48 (10) (1971) 690–691. doi:https://doi.org/10.1021/ed048p690.

[5] F. Panerai, J. D. White, T. J. Cochell, O. M. Schroeder, N. N. Mansour, M. J. Wright, A. Martin, Experimental measurements of the permeability of fibrous carbon at high-temperature, International Journal of Heat and Mass Transfer 101 (2016) 267–273. doi:https://doi.org/10.1016/j.ijheatmasstransfer.2016.05.016.

[6] Y. K. Chen, F. S. Milos, Ablation and Thermal Response Program for Spacecraft Heatshield Analysis, Journal of Spacecraft and Rockets 36 (3) (1999) 1–9. doi:https://doi.org/10.2514/2.3469.

[7] A. J. Amar, B. F. Blackwell, J. R. Edwards, One-Dimensional Ablation Using a Full Newton's Method and Finite Control Volume Procedure, Journal of Thermophysics and Heat Transfer 22 (1) (2008) 71–82. doi:DOI:10.2514/1.29610.

[8] Y.-K. Chen, T. Gökçen, K. T. Edquist, Two-Dimensional Ablation and Thermal Response Analyses for Mars Science Laboratory Heat Shield, Journal of Spacecraft and Rockets (2014) 1–10doi:https://doi.org/10.2514/1.A32868.

[9] H. Weng, A. Martin, Multidimensional Modeling of Pyrolysis Gas Transport Inside Charring Ablative Materials, Journal of Thermophysics and Heat Transfer 28 (4) (2014) 583–597. doi:https://doi.org/10.2514/1.T4434.

[10] M. Wang, Z. Li, Simulations for gas flows in microgeometries using the direct simulation Monte Carlo method, International Journal of Heat and Fluid Flow 25 (6) (2004) 975–985. doi:https://doi.org/10.1016/j.ijheatfluidflow.2004.02.024.

[11] H. Weng, A. Martin, Numerical Investigation of Thermal Response Using Orthotropic Charring Ablative Material, Journal of Thermophysics and Heat Transfer 29 (3) (2015) 429–438. doi:https://doi.org/10.2514/1.T4576.

[12] A. J. Amar, B. Oliver, B. Kirk, G. Salazar, J. Droba, Overview of the CHarring Ablator Response (CHAR) Code, in: 46th AIAA Thermophysics Conference, American Institute of Aeronautics and Astronautics, Washington D.C., 2016, pp. 1–38. doi:https://doi.org/10.2514/6.2016-3385.

[13] J. Lachaud, N. N. Mansour, A. Ceballos, D. Pejakovic, L. Zhang, J. Marschall, Validation of a volume-averaged fiber-scale model for the oxidation of a carbon-fiber preform, in: 46th AIAA Thermophysics Conference, AIAA, Honolulu, Hawaii, 2011, pp. 2011–2223. doi:https://doi.org/10.2514/6.2011-3640.

[14] P. Schrooyen, K. Hillewaert, T. E. Magin, P. Chatelain, Fully implicit Discontinuous Galerkin solver to study surface and volume ablation competition in atmospheric entry flows, International Journal of Heat and Mass Transfer 103 (2016) 108–124. doi:https://doi.org/10.1016/j.ijheatmasstransfer.2016.07.022.

[15] U. Duzel, A. Martin, Modeling high velocity flow through porous media, in: 58th AIAA Aerospace Sciences Meeting, AIAA Paper 2020-0486, Orlando, FL, 2020. doi:https://doi.org/10.2514/6.2020-0486.

[16] U. Duzel, Development of universal solver for high enthalpy flows through ablative materials, Ph.D. Thesis, University of Kentucky, Lexington, KY (December 2020). doi:https://doi.org/10.13023/etd.2020.417.

[17] S. Whitaker, The method of volume averaging, Vol. 13, Springer, 199.

[18] J. Lachaud, I. Cozmuta, N. N. Mansour, Multiscale approach to ablation modeling of phenolic impregnated carbon ablators, Journal of Spacecraft and Rockets 47 (6) (2010) 910–921. doi:https://doi.org/10.2514/1.42681.

[19] J. Marschall, F. S. Milos, Gas Permeability of Rigid Fibrous Refractory Insulations, Journal of Thermophysics and Heat Transfer 12 (4) (1998) 528–535. doi:https://doi.org/10.2514/2.6372.

[20] J. Marschall, F. S. Milos, Gas permeability of rigid fibrous refractory insulations, in: 32nd AIAA Thermophysics Conference, Vol. 12, Atlanta, Georgia, 1997. doi:https://doi.org/10.2514/6.1997-2479.

[21] A. Borner, F. Panerai, N. N. Mansour, High temperature permeability of fibrous materials using direct simulation monte carlo, International Journal of Heat and Mass Transfer 106 (2017) 1318–1326. doi:https://doi.org/10.1016/j.ijheatmasstransfer.2016.10.113.

[22] C. White, T. J. Scanlon, R. E. Brown, Permeability of ablative materials under rarefied gas conditions, Journal of Spacecraft and Rockets 53 (1) (2016) 134–142. doi:https://doi.org/10.2514/1.A33279.

[23] R. Jambunathan, D. A. Levin, A. Borner, J. C. Ferguson, F. Panerai, Prediction of gas transport properties through fibrous carbon preform microstructures using direct simulation monte carlo, International Journal of Heat and Mass Transfer 130 (2019) 923–937. doi:https://doi.org/10.1016/j.ijheatmasstransfer.2018.11.006.

[24] S. Poovathingal, E. C. Stern, I. Nompelis, T. E. Schwartzentruber, G. V. Candler, Nonequilibrium flow through porous thermal protection materials, part ii: Oxidation and pyrolysis, Journal of Computational Physics 380 (2019) 427–441. doi:https://doi.org/10.1016/j.jcp.2018.02.043.

[25] E. C. Stern, S. Poovathingal, I. Nompelis, T. E. Schwartzentruber, G. V. Candler, Nonequilibrium flow through porous thermal protection materials, part i: Numerical methods, Journal of Computational Physics 380 (2019) 408–426. doi:https://doi.org/10.1016/j.jcp.2017.09.011.

[26] M. Ho, S. Leclaire, J.-Y. Trépanier, M. Reggio, A. Martin, Permeability calculation of a fibrous thermal insulator using the lattice boltzmann method, Journal of Thermophysics and Heat Transfer (2020) 1–4doi:https://doi.org/10.2514/1.T6154.

[27] M. Ho, M. Seif, S. McDaniel, S. Leclaire, M. Reggio, J.-Y. Trépanier, M. Beck, A. Martin, Fluid behavior in stochastic porous structures, in: AIAA Scitech 2021 Forum, 2021, p. 1443. doi:https://doi.org/10.2514/6.2021-1443.

[28] F. Panerai, A. Martin, N. N. Mansour, S. A. Sepka, J. Lachaud, Flow-Tube Oxidation Experiments on the Carbon Preform of a Phenolic-Impregnated Carbon Ablator, Journal of Thermophysics and Heat Transfer 28 (2) (2014) 181–190. doi:https://doi.org/10.2514/6.2013-2769.

[29] C. Zhang, T. E. Schwartzentruber, Robust Cut-cell Algorithms for DSMC Implementations Employing Multi-level Cartesian Grids, Computers and Fluids 69 (2012) 122–135. doi:https://doi.org/10.1016/j.compfluid.2012.08.013.

[30] G. A. Bird, J. Brady, Molecular gas dynamics and the direct simulation of gas flows, Vol. 5, Clarendon press Oxford, 1994.

[31] I. D. Boyd, T. E. Schwartzentruber, Nonequilibrium Gas Dynamics and Molecular Simulation, Vol. 42, Cambridge University Press, 2017.

[32] S. Plimpton, S. Moore, A. Borner, A. Stagg, T. Koehler, J. Torczynski, M. Gallis, Direct simulation monte carlo on petaflop supercomputers and beyond, Physics of Fluids 31 (8) (2019) 086101. doi:https://doi.org/10.1063/1.5108534.

[33] M. A. Gallis, T. Koehler, J. R. Torczynski, S. J. Plimpton, Direct simulation monte carlo investigation of the rayleigh-taylor instability, Physical Review Fluids 1 (4) (2016) 043403. doi:https://doi.org/10.1103/PhysRevFluids.1.043403.

[34] M. Gallis, N. Bitter, T. Koehler, J. Torczynski, S. Plimpton, G. Papadakis, Molecular-level simulations of turbulence and its decay, Physical Review Letters 118 (6) (2017) 064501. doi:https://doi.org/10.1103/PhysRevLett.118.064501.

[35] W. E. Lorensen, H. E. Cline, Marching cubes: A high resolution 3d surface construction algorithm, ACM siggraph computer graphics 21 (4) (1987) 163–169. doi:https://doi.org/10.1145/37402.37422.

[36] R. P. Nance, D. B. Hash, H. A. Hassan, Role of Boundary Conditions in Monte Carlo Simulation of Microelectromechanical Systems, Journal of Thermophysics and Heat Transfer 12 (3) (1998) 447–449. doi:https://doi.org/10.2514/2.6358.

[37] Y. Fang, W. Liou, Microfluid flow computations using a parallel dsmc code, in: 40th AIAA Aerospace Sciences Meeting & Exhibit, 2002, p. 1057. doi:https://doi.org/10.2514/6.2002-1057.

[38] A. G. Dumanlı, A. H. Windle, Carbon fibres from cellulosic precursors: a review, Journal of Materials Science 47 (10) (2012) 4236–4250. doi:https://doi.org/10.1007/s10853-011-6081-8.

[39] A. Beskok, G. E. Karniadakis, Report: a model for flows in channels, pipes, and ducts at micro and nano scales, Microscale thermophysical engineering 3 (1) (1999) 43–77. doi:https://doi.org/10.1080/108939599199864.

[40] A. S. Ziarani, R. Aguilera, Knudsen's permeability correction for tight porous media, Transport in porous media 91 (1) (2012) 239–260. doi:https://doi.org/10.1007/s11242-011-9842-6.

[41] D. Dixit, R. Pal, G. Kapoor, M. Stabenau, Lightweight composite materials processing, in: Lightweight ballistic composites, Elsevier, 2016, pp. 157–216. doi:https://doi.org/10.1016/B978-0-08-100406-7.00006-4.

[42] B. K. Bessire, T. K. Minton, Decomposition of phenolic impregnated carbon ablator (pica) as a function of temperature and heating rate, ACS applied materials & interfaces 9 (25) (2017) 21422–21437. doi:https://doi.org/10.1021/acsami.7b03919.

Appendix A. Comparison with experimental dataset

The appendix contains the comparison of the permeability force between DSMC simulations and experimental dataset of Panerai et al [5]. The permeability force for experiments is computed from K_o and b provided in Table 1

of Ref. [5]. Panerai et al. report data for two samples with the same sample density of 181 kg m^{-3} with very different effective permeability (sample TT04 and TT09 in Table 1 of Ref. [5]). Comparison is performed only with sample TT04 (see Sec. 3.1 and Table 2 for discussion).

Table A.3: Permeability force obtained from DSMC simulations is compared to the experimental dataset of Panerai et al. [5]. The error is computed as abs(F_{dsmc}-$F_{expt.}$)/F_{dsmc}*100.

FiberForm Density (kg m^{-3})	**T (K)**	**P_{avg} (Pa)**	**F_{dsmc} (N)**	**F_{expt} (N)**	**Absolute Error (%)**
192	298	251.63	1.09E-07	9.40E-08	15.96
		500.32	1.05E-07	1.05E-07	0.00
	723	502.89	3.46E-07	2.39E-07	44.77
	1123	503.58	6.08E-07	4.73E-07	28.54
	1503	503.32	9.06E-07	7.74E-07	17.05
187	297	477.51	1.16E-07	1.17E-07	0.85
	933	499.02	3.98E-07	4.00E-07	0.50
		251.80	4.98E-07	3.84E-07	29.69
182	361	503.00	1.49E-07	1.55E-07	3.87
		251.99	1.44E-07	1.39E-07	3.60
	1121	503.66	6.28E-07	5.41E-07	16.08
181	297	503.48	1.18E-07	1.19E-07	0.84
	723	503.66	3.60E-07	2.78E-07	29.50
		251.98	3.62E-07	2.64E-07	37.12
189	391	503.28	1.60E-07	1.52E-07	5.26
	823	503.61	4.08E-07	3.13E-07	30.35
		252.05	4.14E-07	3.00E-07	38.00
178	297	503.44	1.18E-07	1.27E-07	7.09
		251.84	1.13E-07	1.11E-07	1.27
	523	503.47	2.35E-07	1.99E-07	18.33
		251.84	2.35E-07	1.83E-07	28.12

Table A.3 – continued from previous page

ρ_F **(kg m^{-3})**	**T (K)**	$\mathbf{P}_{avg}$ **(Pa)**	$\mathbf{F}_{dsmc}$ **(N)**	$\mathbf{F}_{expt}$ **(N)**	**Absolute Error (%)**
186	310	517.08	1.13E-07	1.15E-07	1.53
		267.56	1.09E-07	1.03E-07	5.90
	503	503.51	2.14E-07	1.79E-07	19.28
		264.40	2.14E-07	1.66E-07	29.10
	940	553.41	4.18E-07	4.26E-07	1.82
		267.46	4.83E-07	4.11E-07	17.47
	1320	503.32	7.61E-07	7.19E-07	5.85
		251.84	7.81E-07	7.06E-07	10.65
177	298	503.40	1.22E-07	1.56E-07	22.12
	523	503.54	2.41E-07	2.25E-07	6.91
	731	503.48	3.71E-07	4.16E-07	10.91
	935	503.41	5.09E-07	5.41E-07	5.92
	1130	503.46	6.58E-07	6.57E-07	0.16
		251.86	6.68E-07	6.42E-07	4.07
	1321	503.41	8.06E-07	8.34E-07	3.31
	1507	503.48	9.61E-07	1.08E-06	11.19